PNAS
www.pnas.org

Supplementary Information for

Tough, aorta-inspired soft composites

Chengyang Mo, Haiyi Long, Jordan R. Raney

raney@seas.upenn.edu

This PDF file includes:

Supplementary text
Figs. S1 to S18 (not allowed for Brief Reports)
Legend for Movie S1
SI References

Other supplementary materials for this manuscript include the following:

Movie S1

Supporting Information Text

Rheological properties of PDMS-GF ink. PDMS-GF composite inks with all volume fractions were characterized using a commercial rheometer (TA Instruments Discovery HR 20). Shear-rate ramp and amplitude sweep tests were conducted at room temperature using a 25 mm flat parallel plate with 500 µm gap distance. The shear rate ramp tests show shear thinning behavior of the ink for all volume fractions (Fig. S1a). Data from the amplitude sweep tests show a sharp viscoelastic yield stress for inks of all volume fractions (Fig. S1b). These observations confirm the suitability of the PDMS-GF inks for DIW 3D printing.

Fiber orientation measurements. The local fiber orientation in the printed composites is measured by using images from an optical microscope (see example images in Fig. S2). OrientationJ (1) is used to extract orientation data from the images. We use a pixel radius of 2 with cubic-spline method to calculate the gradient. The color overlay added to the right column of Fig. S2 indicates the local fiber orientation as extracted by the algorithm. This process also computes the orientation distribution, as shown in Fig. S3a. Specifically, the unidirectional composites show a peak orientation around 0° (i.e., parallel with the print direction) while composites printed with a helical shear field have shifted orientation peaks. The effect of nozzle rotation on the distribution of fiber orientation can be clearly seen, with the peak shifting towards the calculated angle from the non-dimensional parameter calculated from printing parameters. The image is taken from the top of the surface, revealing only a portion of the fibers below the surface, suggesting that the majority of the fibers just below the surface will reach the maximum rotation relative to the printing direction.

Following the definition of the HGO model (2), the anisotropy of the fiber reinforcement can be defined by a single parameter κ, called the dispersion parameter, which is defined as:

$$\kappa = -\frac{1}{4}\int_{-pi/2}^{\pi/2} \rho(\phi)\sin^3\phi d\phi \qquad [1]$$

where $\rho(\phi)$ is the fiber orientation distribution. The fibers are unidirectionally aligned when the dispersion parameter is zero. The dispersion parameter increases as fibers are less unidirectionally aligned and more isotropic. Using this formula, the dispersion parameter for three composites printed with different nozzle rotation rates is plotted in Fig. S3b.

Effect of volume fraction. The effects of volume fraction on the tensile properties of PDMS-GF composites have been studied previously (3). Here we also show the effect of volume fraction on the fracture behavior of the composites in Fig. S4. We uniaxially tested composites with five different volume fractions ranging from 5 vol.% to 15 vol.%, giving the stress-stretch curves shown in Fig. S4a. We observed increasing stiffness with increasing vol.% (Fig. S4b), similar to previous observations (3). A ductile-to-brittle transition is also observed above 5 vol.% (Fig. S4c), which can be attributed to the damage mechanism of fiber-matrix debonding (3). The fracture behavior of notched samples is shown in Fig. S4d. Unlike stiffness, there is not a monotonic trend in either toughness (Fig. S4e) or critical stretch (Fig. S4f). The critical stretch is maximized at 10 vol.% at 1.31. At 15 vol.%, the critical stretch of the composites is the same as that of 5 vol.% composites. These results suggest that fiber content does not fully dictate the toughness of the composite. The major contribution to toughness originates from fiber pullout and matrix fracture in our composites. The toughness value for fiber fracture and fiber-matrix debonding is relatively low (G for glass is ~ 10 J/m^2 and G_{ic} for the glass-PDMS interface is ~ 1 J/m^2) (4). The contribution from fiber pullout is linearly related to the volume fraction. However, at larger volume fractions, the mean distance between fibers become much smaller leading to higher stress concentrations in the matrix around fibers after debonding. This leads to premature failure leading to lower toughness, since not all fibers can pullout from the matrix prior to failure.

Effect of fiber treatment. The influence of the bonding strength between fiber and matrix on the mechanical properties of the composite is examined here. The interfacial bonding strength is manipulated by the surface treatment of the fibers using sulfuric acid. The stress-stretch curves for unnotched specimens with various nozzle rotations and volume fractions are shown in Fig. S5a-c. For all nozzle rotations, the 5 vol.% composites lose ductility (with stretch at rupture λ_R changing from ~ 2.5 to ~ 1.5) while the yield stress is significantly increased. However, significant softening is still observed at a stretch around 1.25 for composites with acid-treated fibers. At 10 vol.%, the ductility of the composites is unaffected by the acid treatment. However, the softening is delayed leading to a higher yield stress. Importantly, for both high and low volume fractions, the initial stiffness of the composite remains unchanged for all nozzle rotations, suggesting that the acid treatment of the fibers does not significantly physically degrade the fibers (Fig. S5d).

Next we investigate the effect of fiber treatment on the toughness of the composites by testing specimens that have been pre-cut with a notch perpendicular to the direction of printing. The stress-stretch plots for these notched specimens are shown in Fig. S5e-g. The acid treatment results in a larger critical stretch λ_c and a higher toughness (Fig. S5h). The improvement in toughness is nearly 100% for specimens with 5 vol.% of acid-treated fibers with no rotation, and approximately 33% for specimens with 10 vol.%. Again, at higher volume fraction, the distance between fibers is reduced leading to higher stress concentrations when voids are generated due to fiber matrix debonding. As a result, the failure occurs earlier as cracks form in the matrix between voids, an effect which is controlled by the fracture properties of the matrix. This is why at higher volume fraction, the improvement in toughness is less significant. Moreover, at other nozzle rotations, the toughness of the composites is also improved regardless of volume fraction.

Effect of fiber length. In addition to the glass fibers used in the main text (Fibre Glast, nominal length of 1/16"), we also printed PDMS-GF composites with shorter glass fibers (Fibre Glast, nominal length of 1/32") to investigate the effect of fiber length on the mechanical and fracture properties of the composites. Note, the printed composites include a distribution of fiber lengths due to fiber breakage during ink mixing. We mixed the shorter glass fibers with PDMS using the same procedures described in the main text. We first plot the tensile response of the composites printed with various vol.% and fiber lengths in Fig. S9a. The composites printed with shorter fibers have a lower stiffness than composites printed with longer fibers for a given volume fraction, as shown in Fig. S9b. This drop in stiffness could result both from increased misalignment of the fibers (since fillers with smaller aspect ratios experience less shear stress as they pass through the nozzle, and therefore align less well) and from less transfer of shear stress (again due to the lower aspect ratio). The effect of misalignment is evident by testing the tensile properties of the composites perpendicular to the direction of printing, as shown in Fig. S10a. In this transvere loading case, the composites printed with the shorter (1/32") glass fibers consistently have higher stiffness than composites printed with longer fibers at all vol.%. We note, however, that there is a practical upper limit on the length of fibers that are printable using DIW. The mixing process is more likely to break larger fibers than smaller fibers, reducing the average of the length distribution when large fibers are placed in the ink. Shorter fibers also lead to lower toughness, as shown in Fig. S9d.

Fatigue characterization. To obtain the fatigue threshold for the composites, we conducted cyclic tests (up to 40,000 cycles) at various stretch amplitudes. For each amplitude, two types of samples were tested: one without pre-existing cracks (to measure the strain energy density as a function of cycle number), and the other with a pre-existing crack (to measure crack growth as a function of cycle number). For each type of composite, we performed the fatigue tests at sufficiently-low amplitudes to ensure no observable crack growth up to 15,000 cycles, confirming the existence of the fatigue threshold.

The crack growth rate was calculated with a moving window of 300 cycles over all cycles, quantifying the crack growth rate (da/dN) vs. cycle number (N). Combining this with the strain energy density (W) vs. N, we computed the applied energy release rate (G) vs. crack growth da/dN. For each sample, we only considered crack growth after 50 cycles, since the initial rate of crack growth can be influenced by the manner in which the notch is created. Most samples fail rapidly as the crack grows to a size larger than half the sample width. We also did not use the crack growth rate for the later stage of crack growth, since the approximation of applied energy release rate is no longer valid when the crack reaches significant length.

For both composites with unidirectional alignment and aorta-inspired heterogeneity, we conducted cyclic tests with various stretch amplitudes. The fatigue response of 5 vol.% unidirectional composites is summarized in Fig. S12. The stretch amplitudes for composites with untreated fibers are $\lambda_{max} = 1.10$, 1.15, and 1.20, while those for composites with acid-treated fibers are $\lambda_{max} = 1.15$, 1.20, and 1.25. The lower amplitudes for both composites were chosen such that the samples did not fail after a large number of cycles (no less than 15,000 cycles). The fatigue response in terms of the strain energy density vs. cycle number for the untreated composites is shown in Fig. S12a. As shown in Fig. S12b, no crack growth is observed prior to 15,000 cycles at the stretch amplitude $\lambda_{max} = 1.10$. The crack growth rate is extracted and then plotted vs. the applied energy release rate for each stretch amplitude in Fig. S12c. The fatigue threshold is then extracted by linearly fitting all data points with a growth rate above 0.5 µm/cycle (other than the excluded data described above). Analogous plots are shown for composites with treated fibers in Fig. S12d-f. For the composites with acid-treated fibers, the amplitude for slow crack growth increase from 1.10 to 1.15. No crack growth is observed prior to 25,000 cycles, as shown in Fig. S12e. The fatigue threshold is extracted (Fig. S12f) following the same method used for composites with untreated fibers.

The fatigue response of 10 vol.% aorta-inspired composites is summarized in Fig. S13. The amplitude for slow crack propagation is 1.15 and 1.20 for untreated and acid-treated composites, respectively. The aorta-inspired composites with untreated fibers did not fail until 15,000 cycles at amplitude $\lambda_{max} = 1.15$. The crack growth rate is plotted in Fig. S13c where the fatigue threshold is extracted by a linear fit. The acid treatment further improves the fatigue response of the composites, with no crack propagation observed for stretch amplitude $\lambda_{max} = 1.20$ even after 20,000 cycles (Fig. S13e). For unidirectional composites, this stretch amplitude caused complete failure of the specimens after 7,000 cycles (Fig. S12e). We again plot the crack growth rate vs. applied energy release rate and extract the fatigue threshold (Fig. S13f) of the aorta-inspired composites with acid-treated fibers.

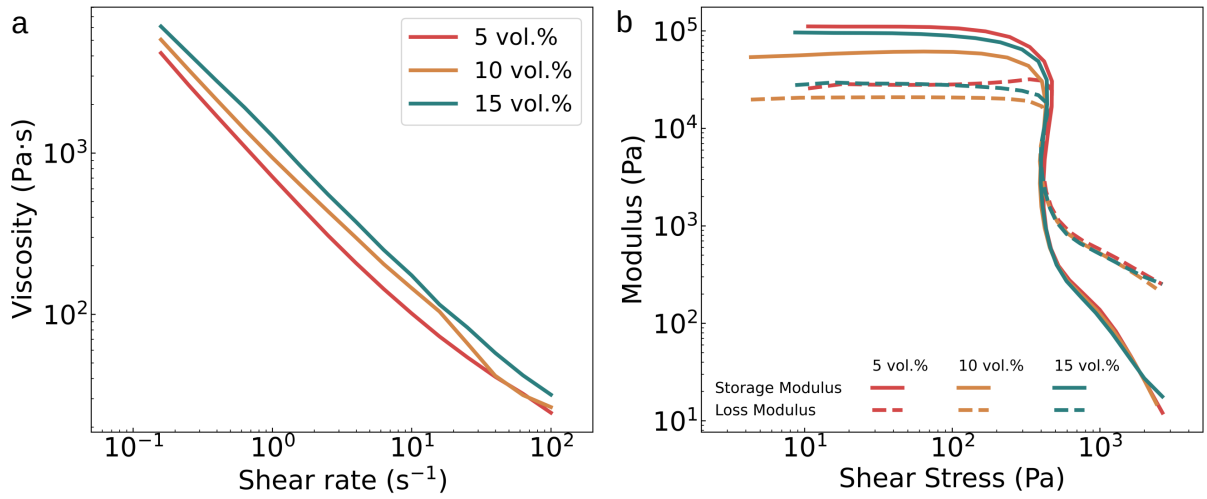

Fig. S1. Rheological characterization of PDMS-GF inks with various volume fractions of fibers. (a) Plotting viscosity versus shear rate reveals shear-thinning behavior for all inks. (b) Amplitude sweep tests show the existence of a sharp viscoelastic yield stress for all inks, as desirable for DIW printing.

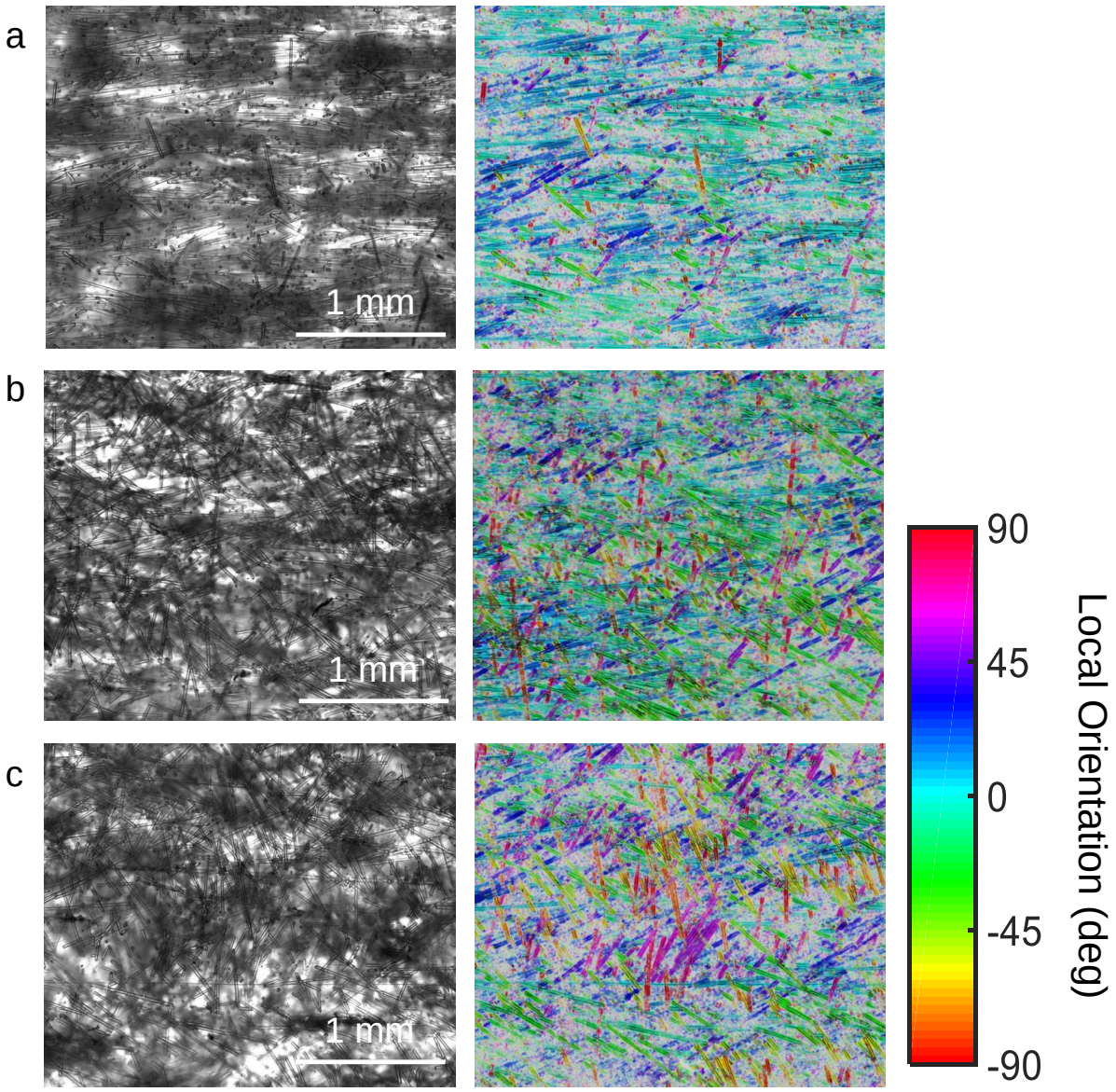

Fig. S2. Surface optical microscope image of printed PDMS-GF composites with nozzle rotation. The overlaid false color maps in the right column indicate the local orientation of the fibers, calculated using OrientationJ. (a) $\varphi = 0^\circ$, (b) $\varphi = 20^\circ$, (c) $\varphi = 40^\circ$

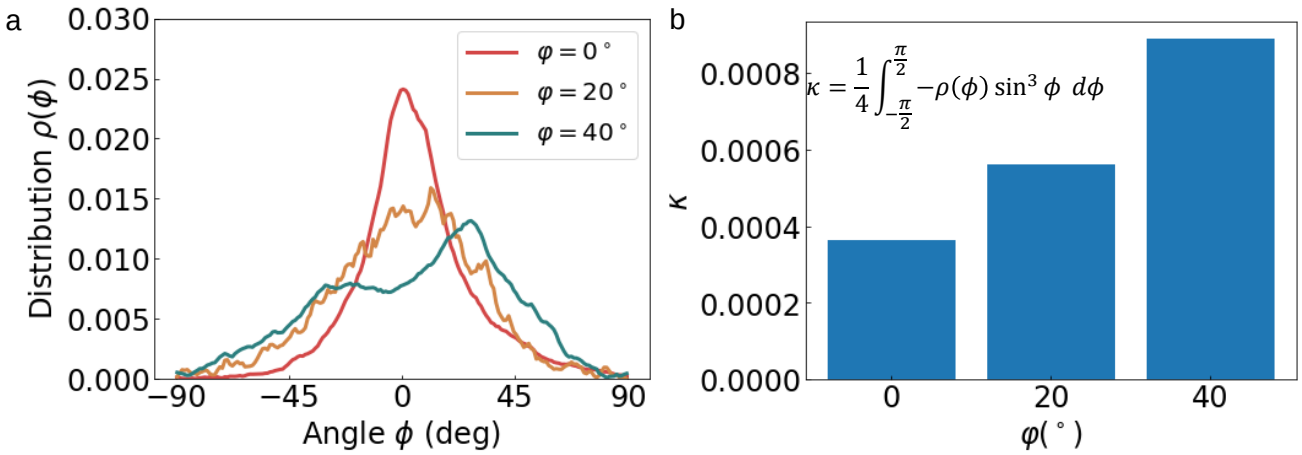

Fig. S3. (a) Orientation distribution calculated from the false color maps in Fig. S2 for various idealized rotation angles φ. (b) Orientation dispersion as calculated using Eq. 1 for various idealized rotation angles.

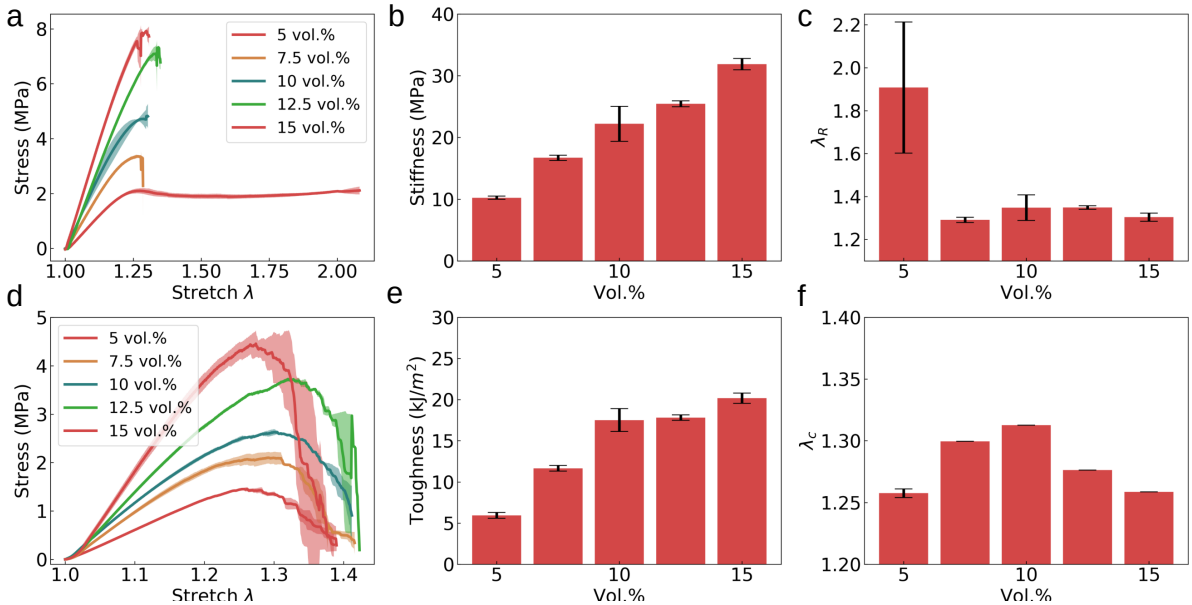

Fig. S4. Effect of fiber volume fraction on the mechanical properties of unidirectional PDMS-GF composites. (a) Experimentally-measured stress-stretch behavior of unnotched specimens; (b) the stiffness and (c) stretch of rupture of composites with various volume fractions; (d) experimentally-measured stress-stretch behavior of notched specimens; (e) toughness and (f) critical stretch of composites with various volume fractions.

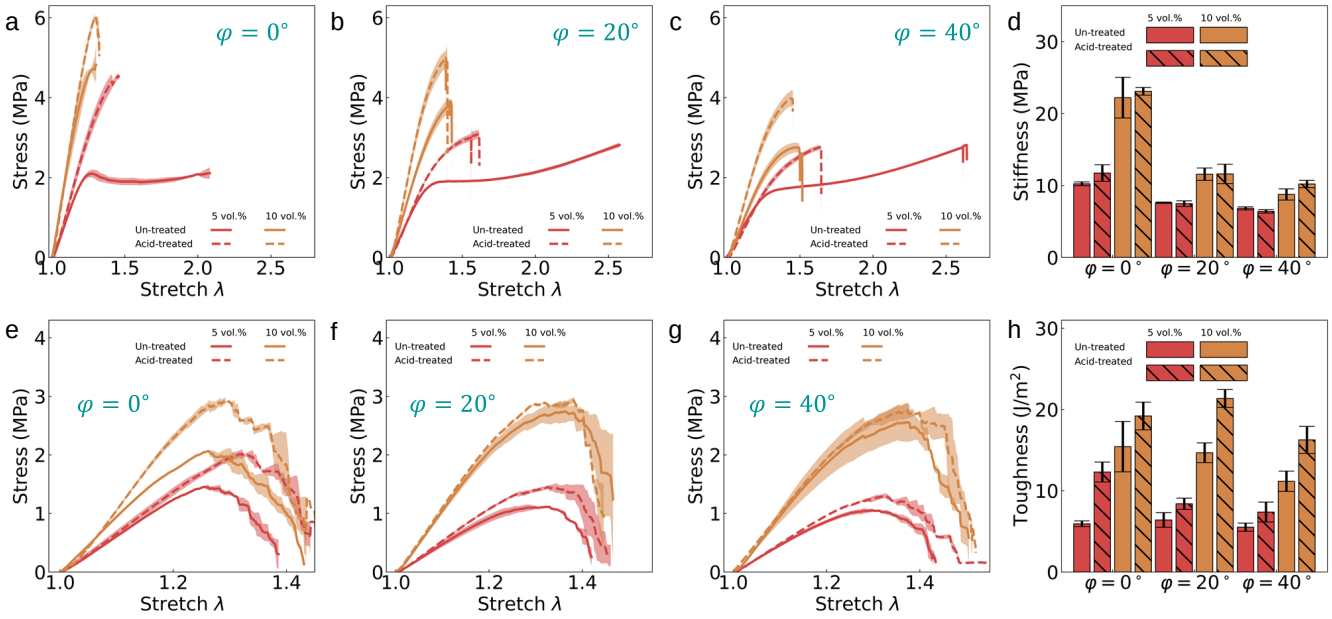

Fig. S5. Effect of fiber treatment on the mechanical properties of PDMS-GF composites. (a)-(c) Experimentally-measured stress-stretch behavior of unnotched PDMS-composites with various idealized fiber angles; (d) Stiffness of composites with various idealized fiber orientations, volume fractions, and fiber treatments; (e)-(g) stress-stretch relationship for notched PDMS composites with various idealized fiber orientations; (h) toughness of composites with different idealized fiber orientations, volume fractions, and fiber treatments.

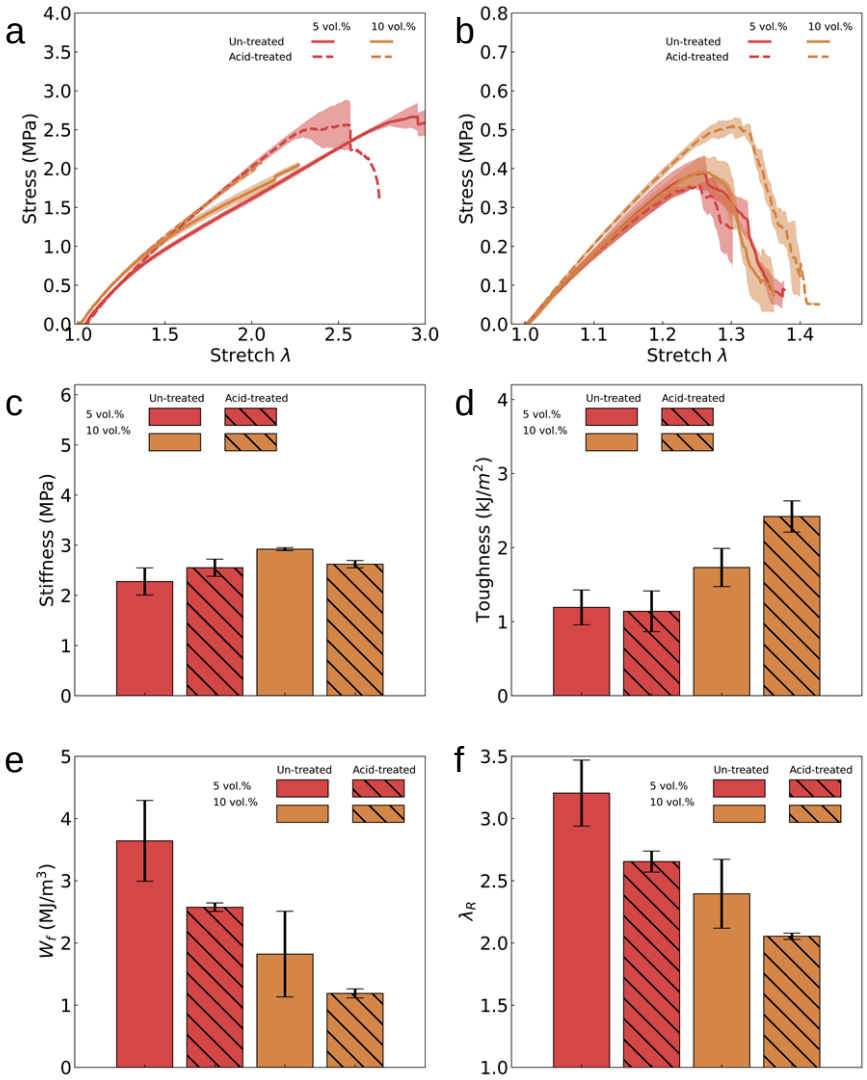

Fig. S6. Tensile and fracture properties of PDMS-GF composites subjected to transverse loading (i.e., loading perpendicular to the fiber orientation) as a function of volume fraction and fiber treatment. (a) Measured stress-stretch response of unnotched composites, (b) stress-stretch response of notched composites, (c) stiffness of composites loaded transversely, (d) toughness of composites loaded transversely, (e) work of fracture of composites loaded transversely, (f) stretch of rupture.

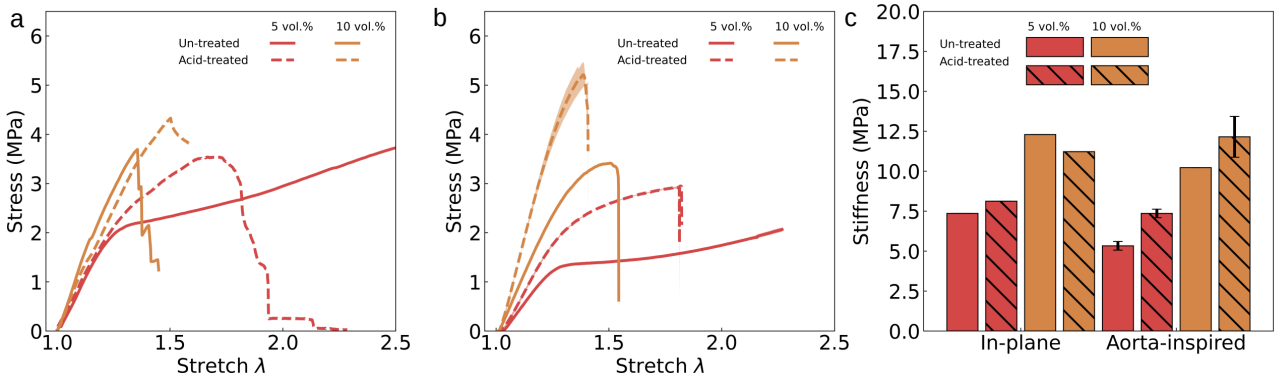

Fig. S7. Measured stress-stretch behavior for unnotched composites with: (a) in-plane heterogeneity and (b) aorta-inspired heterogeneity. (c) Stiffness of composites with heterogeneity and various volume fractions and fiber treatments.

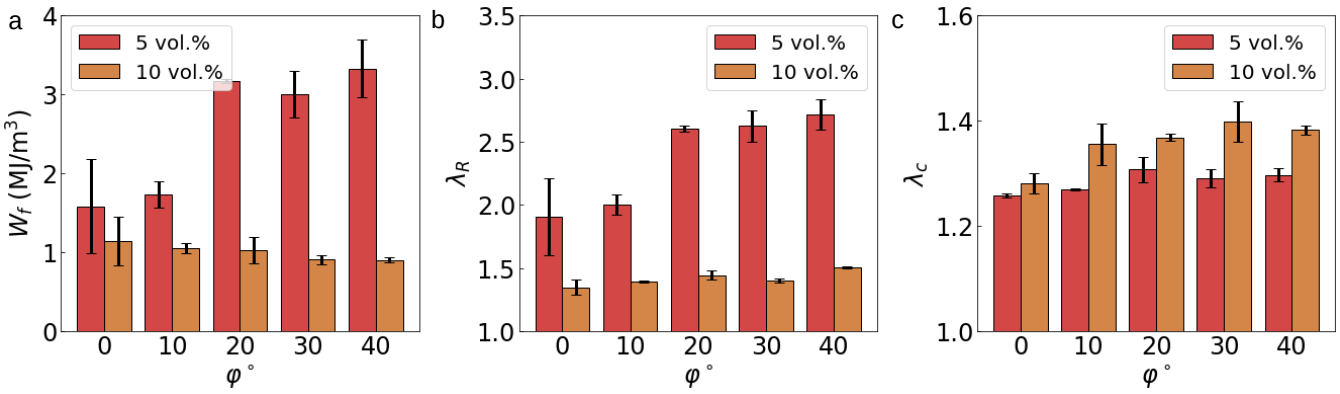

Fig. S8. Additional tensile properties of PDMS-GF composites: (a) Work of fracture (total strain energy density), (b) stretch of rupture, (c) critical stretch.

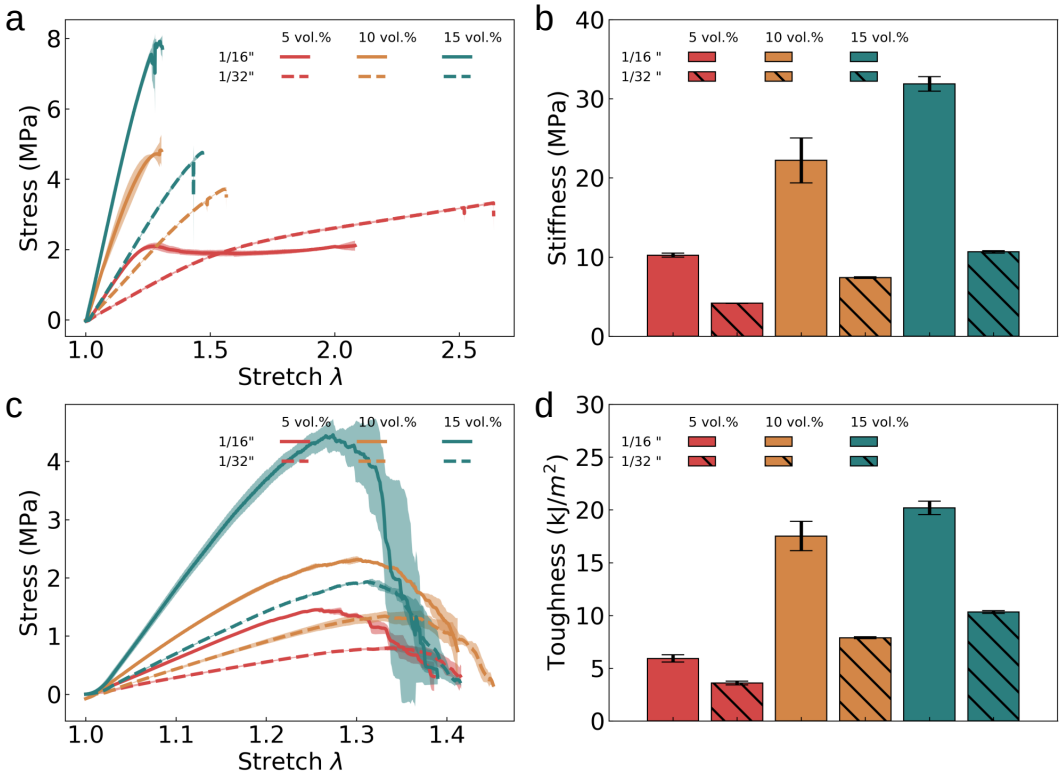

Fig. S9. Effect of fiber length distribution: (a) stress-stretch behavior of unnotched specimens with various vol.% and fiber lengths; (b) stiffness of composites with various vol.% and fiber lengths; (c) stress-stretch behavior of notched specimens with various vol.% and fiber lengths; and (d) toughness of composites with various vol.% and fiber length.

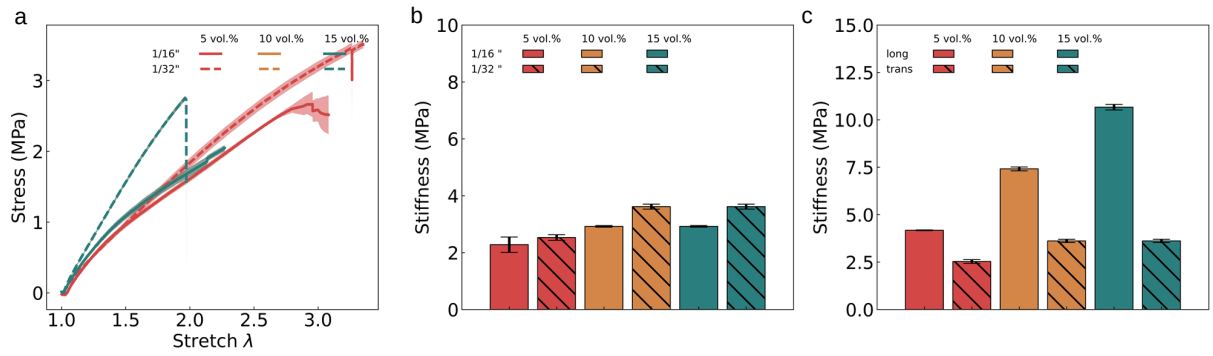

Fig. S10. Effect of fiber length on the tensile properties of composites loaded transversely (perpendicular to the direction of fiber orientation): (a) stress stretch curve of composites with various vol.% and fiber lengths loaded transversely; (b) stiffness of composites with various vol.% and fiber lengths loaded transversely; (c) Anisotropy in stiffness for composites printed with 1/32" glass fibers.

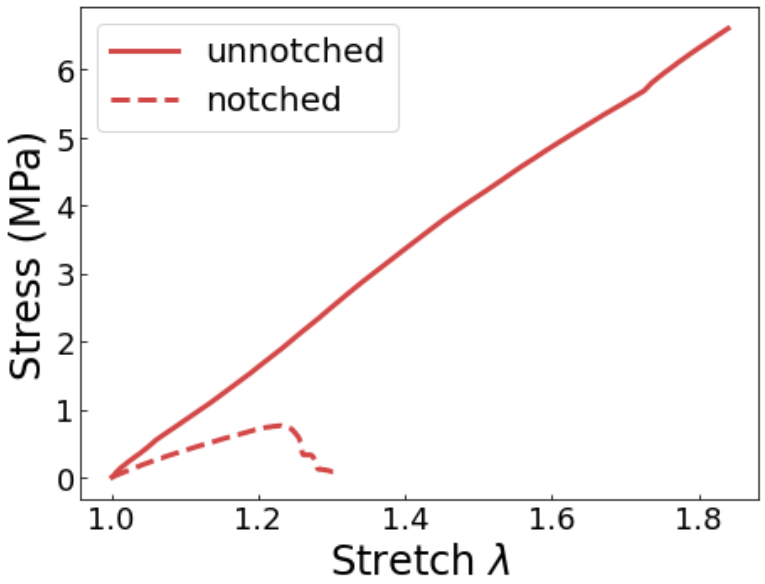

Fig. S11. Measured stress-stretch behavior for unnotched and notched samples of rheologically-modified PDMS for 3D printing.

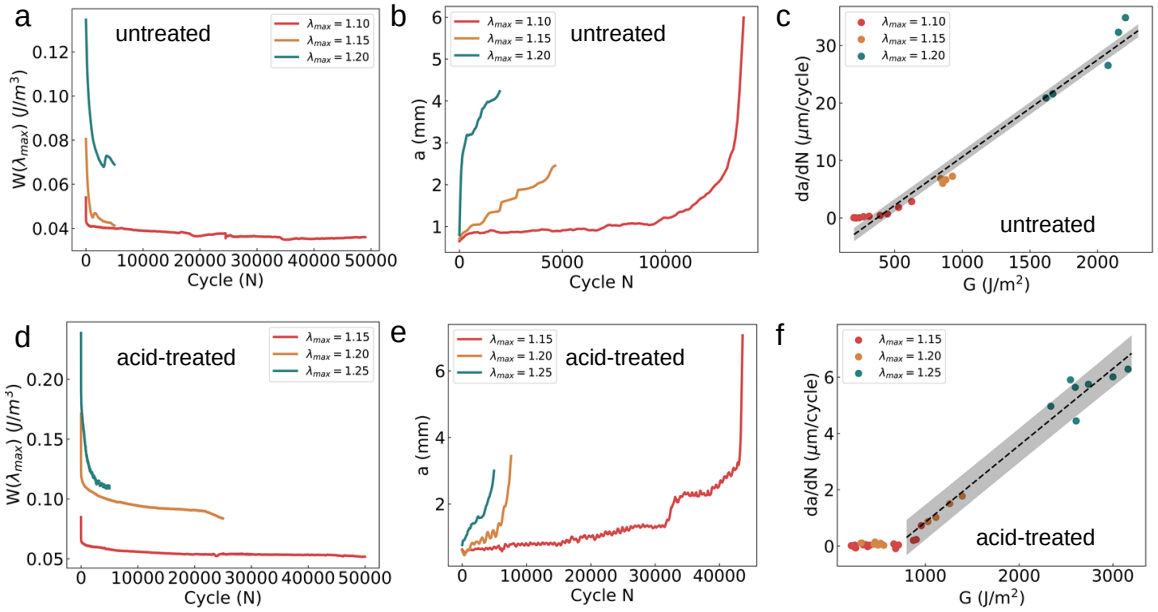

Fig. S12. Fatigue behavior of 5 vol.% unidirectional PDMS composites. (a) Strain energy density of each loading curve of each cycle for composites with untreated fibers. (b-c) Fatigue crack length as a function of cycle number and crack growth rate (da/dN), respectively, as a function of the applied energy release rate for composites with untreated fibers; (d) Strain energy density of each loading curve of each cycle for composites with acid-treated fibers. (e-f) fatigue crack length as a function of cycle number and crack growth rate (da/dN), respectively, as a function of the applied energy release rate for composites with acid-treated fibers.

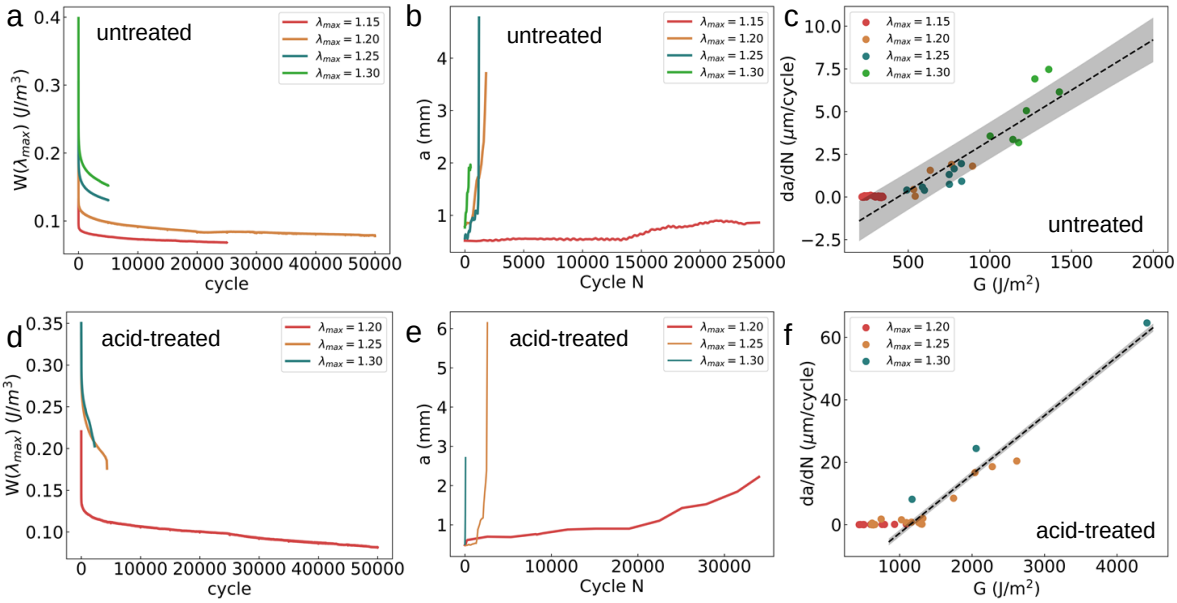

Fig. S13. Fatigue behavior of aorta-inspired composites with 10 vol.% glass fibers. (a) Strain energy density of each loading curve of each cycle for composites with untreated fibers. (b-c) Fatigue crack length as a function of cycle number and crack growth rate (da/dN), respectively, as a function of the applied energy release rate for composites with untreated fibers; (d) Strain energy density of each loading curve of each cycle for composites with untreated fibers; (e-f) fatigue crack length as a function of cycle number and crack growth rate (da/dN), respectively, as a function of the applied energy release rate for composites with acid-treated fibers.

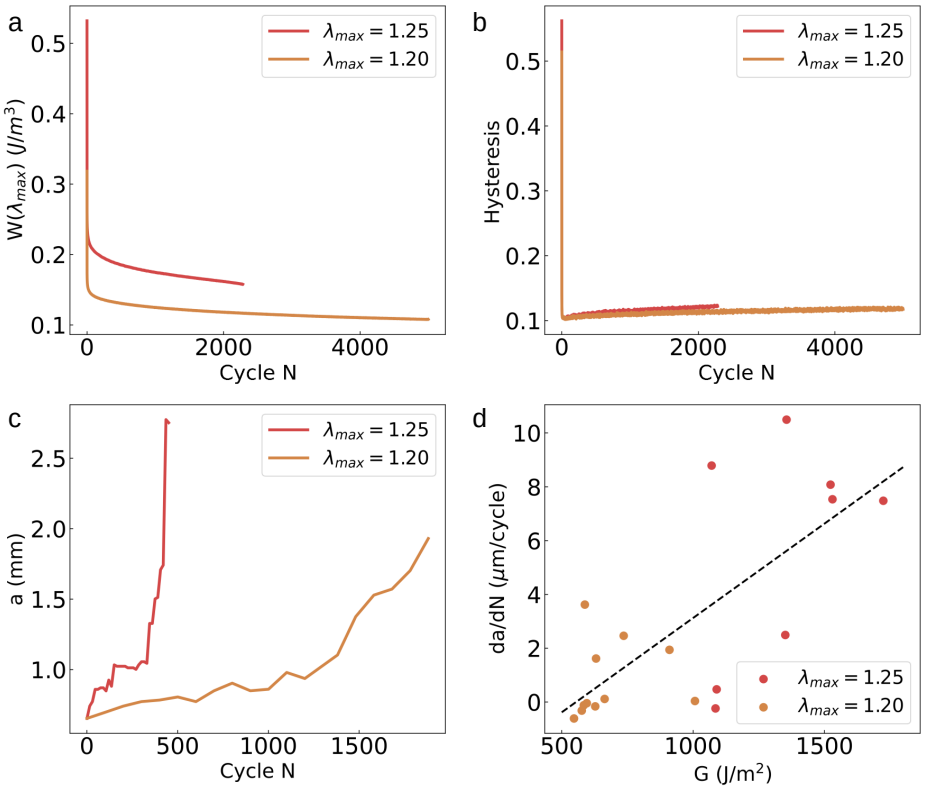

Fig. S14. Fatigue crack growth of 10 vol.% unidirectional composites with untreated fibers. (a-b) Strain energy density and hysteresis, respectively; (c-d) fatigue crack length as a function of cycle number and crack growth rate (da/dN), respectively, as a function of the applied energy release rate for composites with 10 vol.% fibers.

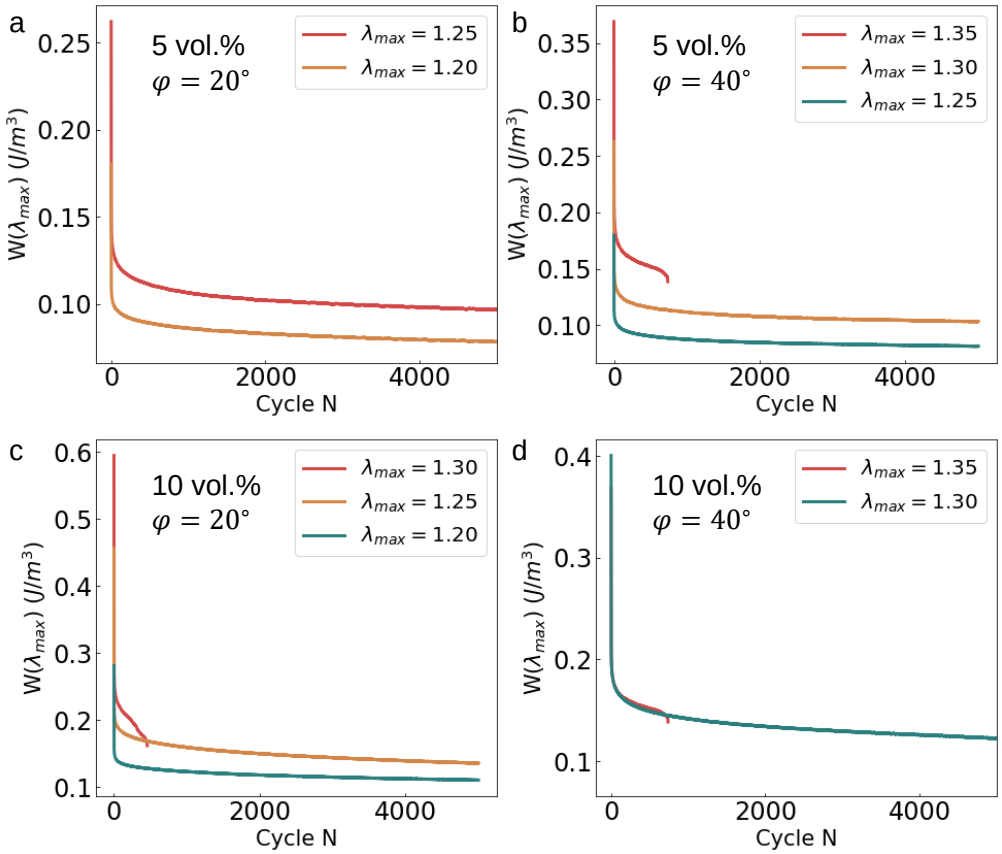

Fig. S15. Fatigue behavior of composites with untreated fibers and without notch, printed with nozzle rotation in terms of strain energy density vs. number of cycles for composites with (a) 5 vol.% fibers and idealized fiber angle $\varphi = 20^{\circ}$; (b) 5 vol.% fibers and idealized fiber angle $\varphi = 40^{\circ}$, (c) 10 vol.% fibers and idealized fiber angle $\varphi = 20^{\circ}$, (d) 10 vol.% fibers and idealized fiber angle $\varphi = 40^{\circ}$.

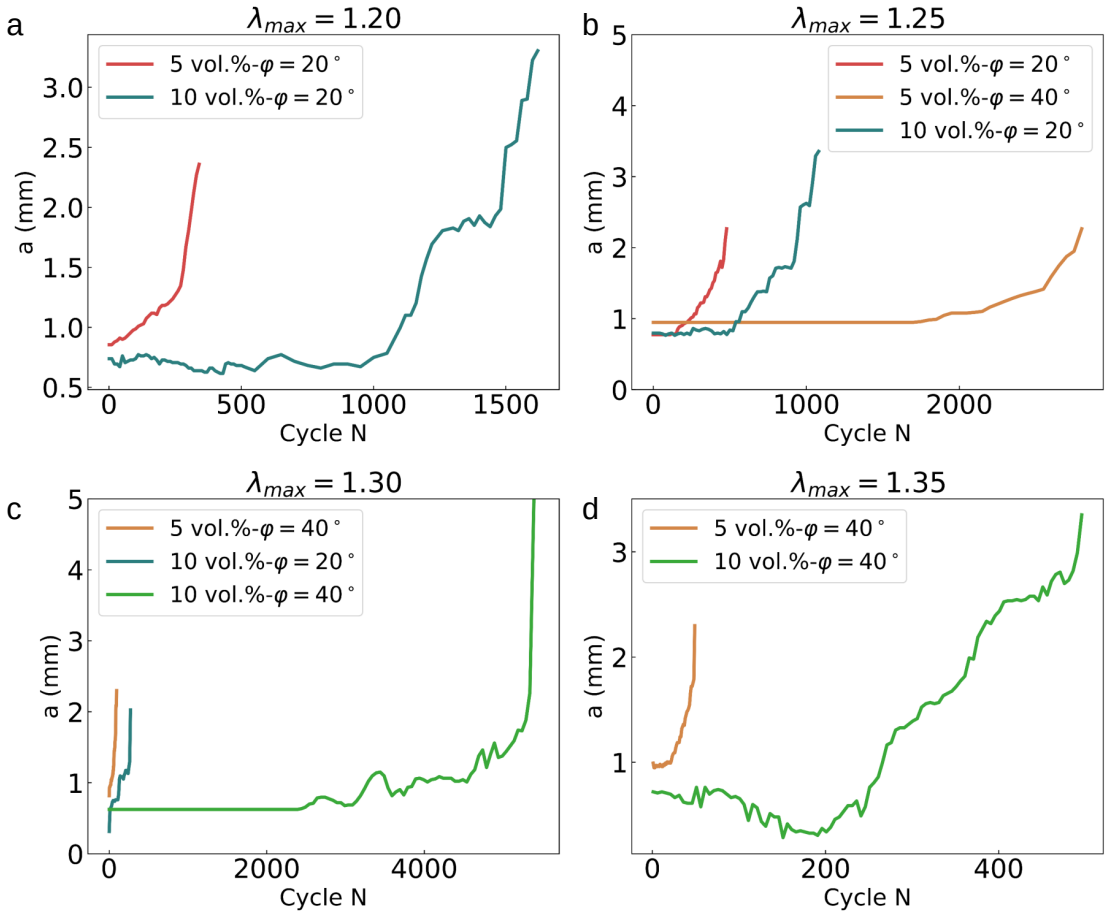

Fig. S16. Fatigue behavior of composites with notch, printed with nozzle rotation. Crack length a vs. number of loading cycles N for stretch amplitudes (a) $\lambda_{max} = 1.20$, (b) $\lambda_{max} = 1.25$, (c) $\lambda_{max} = 1.30$, and (d) $\lambda_{max} = 1.35$.

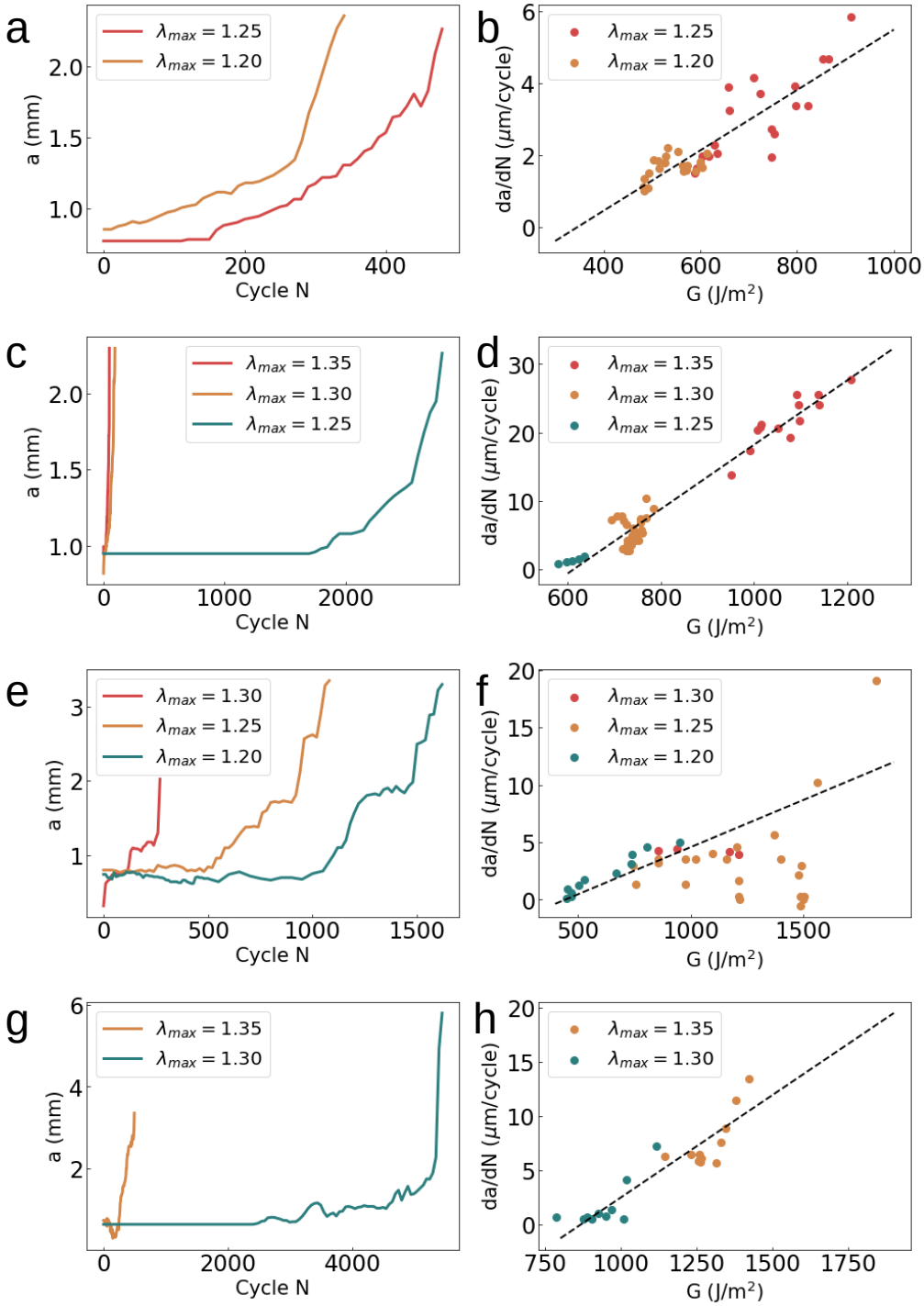

Fig. S17. Fatigue crack growth of composites printed with nozzle rotation. (a-b) Fatigue crack length as a function of cycle number and crack growth rate (da/dN), respectively, as a function of the applied energy release rate for composites with 5 vol.% fibers and idealized fiber angle $\varphi = 20^{\circ}$; (c-d) fatigue crack length as a function of cycle number and crack growth rate (da/dN), respectively, as a function of the applied energy release rate for composites with 5 vol.% fibers and idealized fiber angle $\varphi = 40^{\circ}$; (e-f) fatigue crack length as a function of cycle number and crack growth rate (da/dN), respectively, as a function of applied energy release rate for composites with 10 vol.% fibers and idealized fiber angle $\varphi = 20^{\circ}$; (g-h) fatigue crack length as a function of cycle number and crack growth rate (da/dN), respectively, as a function of applied energy release rate for composites with 10 vol.% fibers and idealized fiber angle $\varphi = 40^{\circ}$.

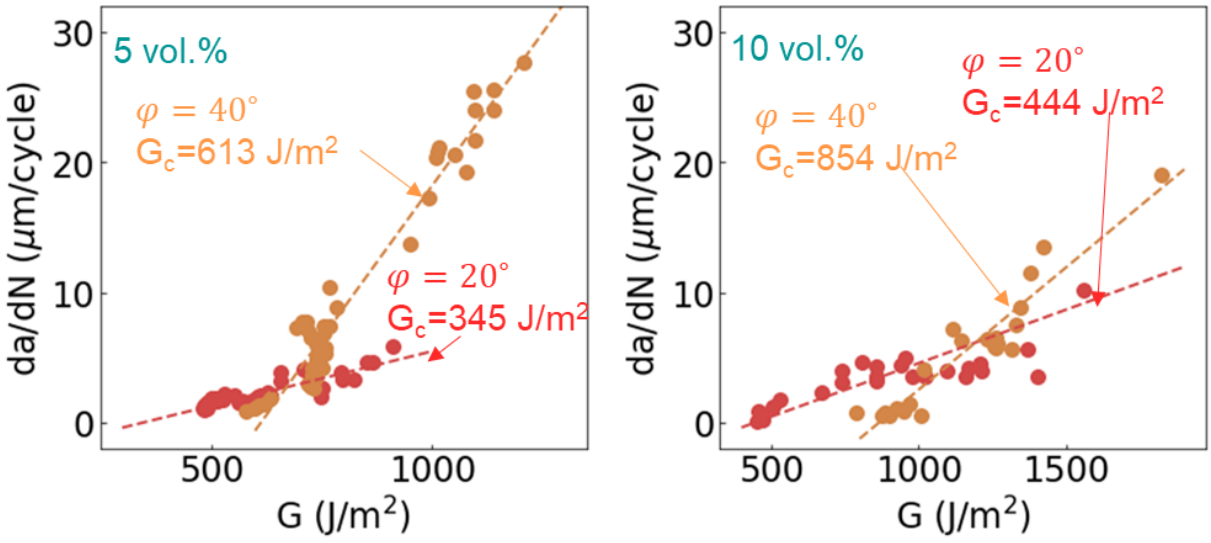

Fig. S18. Determination of fatigue threshold for composites with 5 vol.% and 10 vol.% fibers, respectively, printed with nozzle rotation. The fatigue threshold values are used in Fig. 6b.

Movie S1. Video showing crack propagation of 10 vol.% composites with in-plane heterogeneity.

References

1. R Rezakhaniha, et al., Experimental investigation of collagen waviness and orientation in the arterial adventitia using confocal laser scanning microscopy. *Biomech. Model. Mechanobiol.* **11**, 461–473 (2012).
2. GA Holzapfel, TC Gasser, RW Ogden, A new constitutive framework for arterial wall mechanics and a comparative study of material models. *J. Elast.* **61**, 1–48 (2000).
3. C Mo, Y Jiang, JR Raney, Microstructural evolution and failure in short fiber soft composites: Experiments and modeling. *J. Mech. Phys. Solids* **141**, 103973 (2020).
4. D Hull, TW Clyne, *Toughness of composites*, Cambridge Solid State Science Series. (Cambridge University Press), 2 edition, p. 208–236 (1996).